Material: Ferritic Steel: F82H
Property: Yield Stress & Ultimate Tensile Stress
Data: Experimental
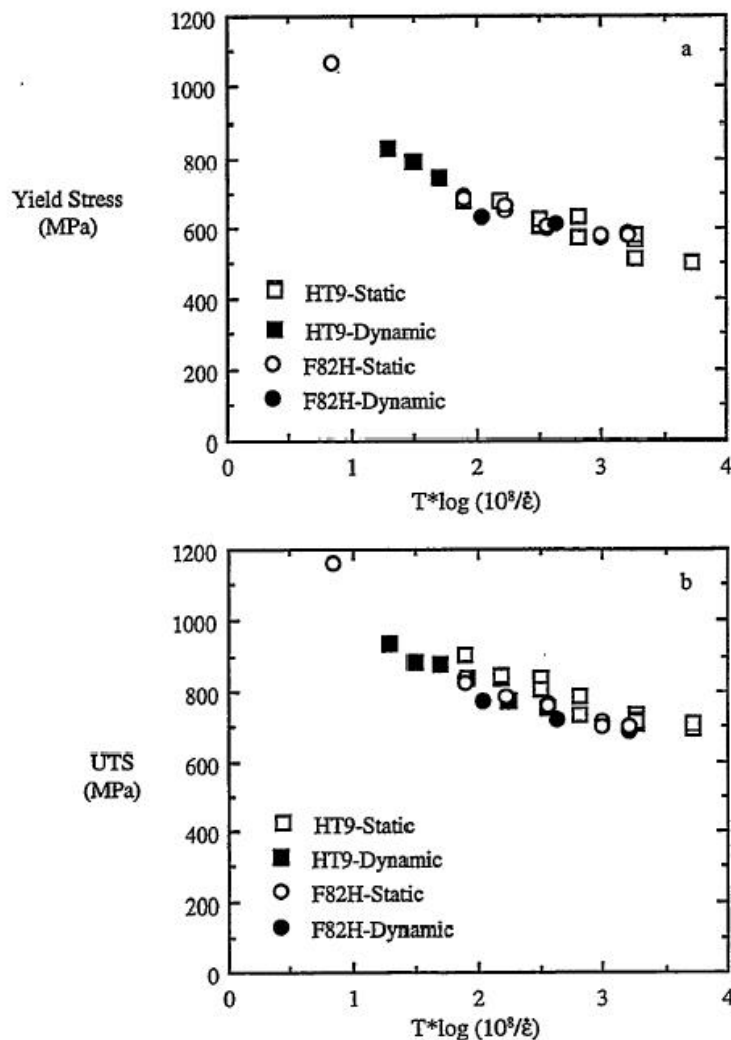

Figure. 1   Comparison of a) yield stresses and b) ultimate tensile strengths of HT9 and F82H as a function of strain rate compensated temperature.
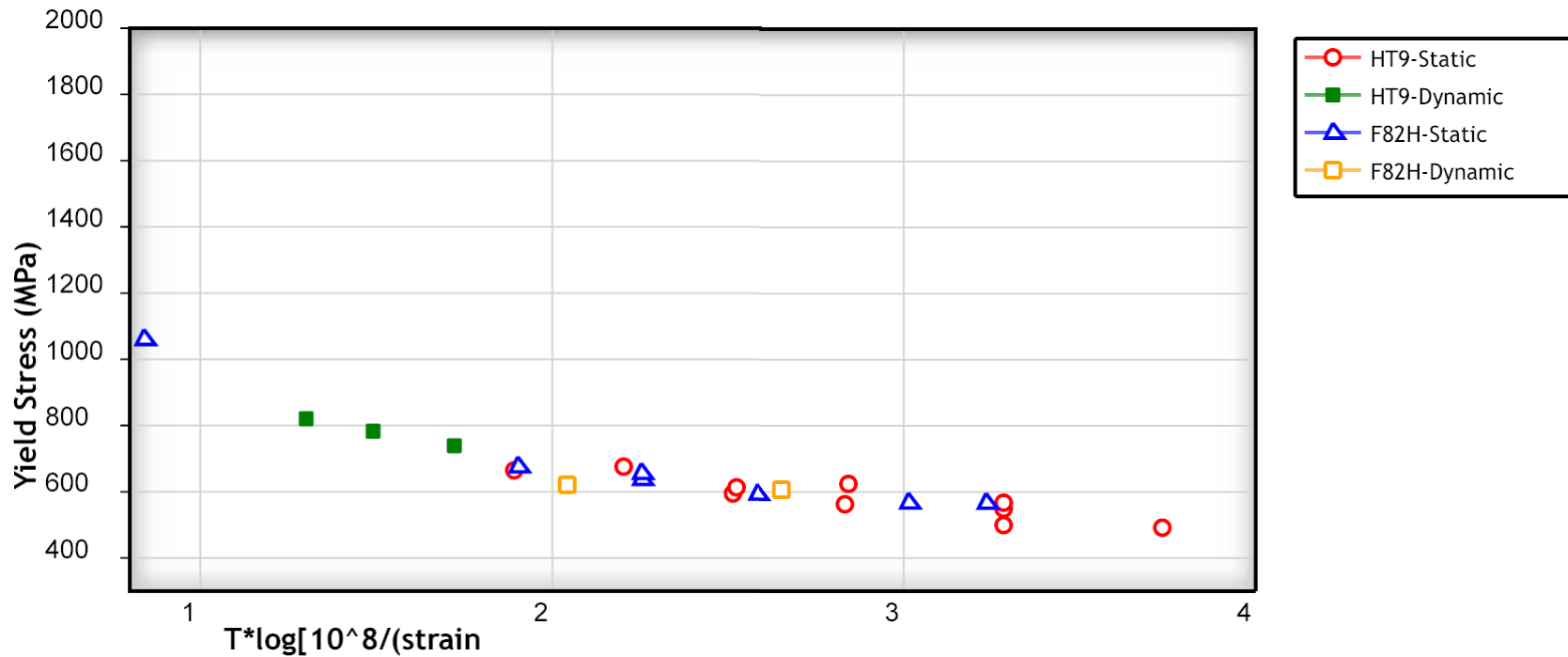
Title of paper (or report) this figure appeared in:
On the Role of Strain Rate, Size and Notch Acuity on Toughness: A Comparison of Two Martensitic Stainless Steels
Author of paper or graph:
G.E. Lucas, G.R. Odette, J.W. Sheckherd, K. Edsinger, B. Wirth

Comparison of yield stresses of HT9 and F82H as a function of strain rate compensated temperature.

Reference:
 Author: *G.E. Lucas, G.R. Odette, J.W. Sheckherd, K. Edsinger, B. Wirth*
   Title: *On the Role of Strain Rate, Size and Notch Acuity on Toughness: A Comparison of Two Martensitic Stainless Steels*
 Source: *Fusion Materials Semi-Annual Progress Reports (March 31, 1995), Volume 18, Page 147-168,* [PDF]

View Data

Author Comments

Plot Format:

  Y-Scale: ⦿ linear ○ log ○ ln
  X-Scale: ⦿ linear ○ log ○ ln

ON THE ROLE OF STRAIN RATE, SIZE AND NOTCH ACUITY ON TOUGHNESS: A COMPARISON OF TWO MARTENSITIC STAINLESS STEELS - G. E. Lucas, G. R. Odette, J. W. Sheckherd, K. Edsinger, B. Wirth (Department of Chemical & Nuclear Engineering and Mechanical Engineering, University of California, Santa Barbara)

OBJECTIVE

Ongoing work is being conducted to characterize the mechanical properties of tempered martensitic (TM) stainless steels. The objective of the present report is to relate observations for two of these steels, HT9 and F82H.

SUMMARY

The fracture resistance and micromechanisms of two tempered martensitic steels were characterized over a range of temperatures by both mechanical testing and quantitative fractography. Both HT-9 and F82H undergo a fracture mode transition from quasi-cleavage at low temperature to microvoid coalescence at high temperature. The transition in HT9 is rather gradual, and the transition in F82H is extremely abrupt. While the toughness of F82H was higher in all cases, differences between the two steels depended on test type, strain rate and temperature. In general F82H had only slightly better properties in the quasi-cleavage regime. For example, the transition temperatures indexed at fracture toughness levels of 100 MPa√m were only 25 and 14°C lower in F82H than HT-9 under static and dynamic conditions, respectively, and they were identical at the 10 J level for Charpy impact tests. However, the fracture resistance of F82H was higher than HT9 in the ductile fracture regime. The Charpy V-notch upper shelf initiation energies in F82H were roughly twice those of HT-9, and total upper shelf energies were three times larger. Differences appeared to be smaller for both static and dynamic upper shelf toughness. Charpy upper shelf energies reflect complex and extrinsically mediated crack tearing processes that have, at best, very limited fundamental or structural significance. Thus, using an energy of 41J, widely perceived to be appropriate indexing a ductile-to-brittle transition temperature (DBTT) for Charpy data, results in a much lower (by 81°C) putative DBTT for F82H compared to HT-9. These results not only demonstrate the inherent non-uniqueness of the so called DBTT, but also call into question the use of Charpy data for ranking the relative performance of various alloys. The similarities in quasi-cleavage fracture and differences in ductile fracture are manifested in the fracture surfaces and are interpreted in terms of the underlying mechanisms and microstructures.

PROGRESS AND STATUS

Introduction

The demonstrated swelling resistance and high heat flux capacity make tempered martensitic (TM) steels a leading candidate alloy class for application to fusion first wall and blanket structures. However, TM alloys undergo

a change from nominally ductile to nominally brittle fracture below a so called ductile-to-brittle transition temperature (DBTT) that may be substantially increased by irradiation. Hence, radiation embrittlement is widely believed to be the major disadvantage of TM steels.

As we have shown elsewhere, however, there is no unique DBTT, and the defect tolerant capabilities of a material must be judged by more structurally relevant measures of strength and strain limits in the presence of cracks.[1,2] Developing and applying appropriate measures requires a more fundamental approach, based on an understanding of underlying fracture processes. To this end we have carried out a comprehensive series of mechanical property tests coupled with detailed fractographic analyses on two leading candidate TM steels which have been, or are being, characterized in a number of irradiation programs. The objective is to compare and contrast various macroscopic and microscopic measures of fracture resistance and to interpret the results both in terms of fundamental mechanisms and structural implications.

Experiment

The two steels examined were HT-9 and F82H. HT9 is a 12Cr-1Mo-W-V steel originally developed for fossil energy plants that has been investigated broadly for both fast reactor and fusion reactor applications.[3] The F82H is an optimized reduced activation 8 Cr-2W-V steel specifically targeted for fusion applications.[4] It is the immediate precursor to a large International Energy Agency (IEA) heat that will be the focus of research on TM alloys in the next several years. [5]

The composition of the electroslag refined (ESR) heat of HT-9 is given in Table 1. After hot rolling at 1050 to 1090°C the ~25 mm thick plate was stress relieved at 850°C for 2 h cooled at 5°C/h to 700°C, held for 6h and air cooled.[6] Previous analysis has shown that this steel has a tempered martensitic structure with prior austenite grains (PAG) of about 55 μm diameter containing martensite laths in packets of about 7-8 μm in diameter.[7] The carbon content of HT-9 is relatively high at 0.23%. The matrix contains a fine scale distribution of Mo_2C and MC precipitates and coarser $M_{23}C_6$ and M_6C carbides. The lath, the lath packet and PAG boundaries are heavily decorated with (mostly $M_{23}C_6$) carbides typically less than 0.2μm in size; there is also a smaller population of relatively large (1μm) carbides along PAG boundaries; the boundary carbides are rich in Cr and contain significant amounts of iron and molybdenum.[6,7]

The composition of the F82H steel, obtained courtesy of A. Hishinuma of Japan Atomic Energy Research Institute, is also shown in Table 1. Nickel, molybdenum and niobium contents have been minimized to achieve reduced neutron activation and tungsten, vanadium and tantalum have been added as replacements — viz., as strong carbide formers and for other metallurgical purposes such as grain size control. The carbon content of

Composition (Wt %)

Steel	C	Mn	Si	Ni	Cr	Mo	V	W	Ta	S	P
HT-9	.23	.39	.17	.51	12.1	1.04	.28	.45	—	.003	.016
F82H	.10	.5	.1	—	8.0	—	.2	2.0	.04	.003	.003

Table 1. Compositions of HT-9 and F82H

F82H, at 0.10%, is significantly lower than in HT9. The material was received as 25 mm thick plate which had been normalized at 1040°C for 0.5 h and tempered at 740°C for 1h. The reported microstructure consists of tempered martensite with a prior austenite grain size of about 120 μm. Boundary and matrix precipitation consists primarily of Cr-rich $M_{23}C_6$. Consistent with the lower carbon content, the boundary carbides tend to be finer (on average ≤ 0.15μm) and less numerous than those observed in the HT-9.[8,9] Although not reported specifically for F82H, microstructures of steels with similar compositions and heat treatments have been observed to contain significant populations of matrix and boundary carbides, which include, depending on steel composition, M_6C (Ta and W-rich) and MC (V and Ta-rich).[10,11]

Round bar tensile specimens 3.2 mm in diameter by 25.4 mm in gage length were cut from the HT-9 plate in the transverse orientation. Flat miniature tensile specimens with gage sections 9 mm x 2 mm x 0.5 mm were punched from coupons cut from the F82H and lapped to 0.5 mm thickness. These miniature tensile specimens have provided data in good agreement with larger specimens.[12] Fracture specimens included standard ASTM E23 blunt-notched Charpy specimens (CVN), subsized Charpy (MCVN) specimens scaled by a factor of one-third in all dimensions, and precracked three-point bend specimens. The three-point bend specimens (3PB) were fatigue pre-cracked at a final $\Delta K \leq 20$ MPa√m to a depth (a) to width (W) ratio of a/W ≈ 0.5. They included full thickness (T) Charpy specimens (PCCV) and 0.2T, 0.4T and 0.6T bend bars. In the case of HT-9, 0.15 to 1T compact tension (CT) and disc compact tension (DCT) test specimens were also included in the test matrix.

Tensile tests on HT-9 were conducted at temperatures ranging from -101°C to 66°C at strain rates in the range 10^{-3} to 3 s^{-1} on a servo-hydraulic load frame. Tensile tests on F82H were performed at strain rates of 10^{-3} s^{-1} over a temperature range of -196°C to 25°C and at 10^{-1} and 10s^{-1} at 25°C. Fracture tests were also carried out over a wide range of loading rates and temperatures from -196 to 350°C. Temperature control was achieved by a number of techniques ranging from a variety of baths to pre-cooling specimen/fixture assemblies. Impact tests were performed on both the CVN and PCCV specimens on an instrumented pendulum impact machine. The MCVN specimens were tested on a drop tower at somewhat lower (~5 times) impact velocities. In all cases load-time data were used to determine both the total and partitioned (e.g., initiation) energies; and for the PCCV specimens, dynamic elastic (K_{Id}) and elastic-plastic toughness (K_{Jd}, assuming crack initiation at maximum

loads).[13] The static, pre-cracked 3PB, CT, and DCT specimens were tested at relatively low displacement rates (~0.008 mm/s) on a servo-hydraulic load frame. Standard ASTM practices were used to determine valid linear elastic toughness, K_{Ic} (ASTM E 399), or critical elastic-plastic energy release rates, JI_c (E 813); in the latter case crack growth (Δa), if any, was measured by unloading compliance (PCCV and 3PB) or electric potential drop (CT, DCT) methods.[14]

Scanning electron microscopy (SEM) and confocal microscopy (CM) were performed on selected specimens to characterize details of the fracture process. The CM was used to generate quantitative, three dimensional topographic maps of the fracture surfaces. Maps of conjugate fracture surfaces were input to a fracture reconstruction (FR) technique to evaluate the damage evolution/fracture sequence-of-events ahead of the crack tip as a function of crack tip opening displacement (d). Details of the CM/FR method are described elsewhere.[15,16]

Results — Mechanical Properties

Tensile and Charpy Tests- - Uniaxial yield stress σ_y and ultimate tensile strength (UTS) are plotted in Figure 1 against a strain rate ($\dot{\varepsilon}$) compensated temperature parameter, $P_T = T(K)\log(10^8/\dot{\varepsilon})$. Although not a unique way of correlating tensile properties to temperature and strain rate, P_T has been found useful for other steels [17] and reasonably collapses the dynamic to static data for both HT9 and F82H. In spite of differences in composition and heat treatments, the strengths of these two steels are quite similar (note, on average the UTS for the HT9 is about 50 MPa higher than for the F82H). The uniform elongations (not shown) ranged from about 12% at room temperature to 15% at -100°C in the HT9, and from about 7% at room temperature to 10% at -100°C in the F82H. The strain hardening behavior was also similar, with strain hardening exponents of about 0.1 to 0.15.

Total absorbed energy (E)-temperature (T) data for the Charpy impact tests are shown in Figure 2a. The HT9 shows a very broad transition from lower shelf (ending at about -100°C) to an upper (beginning at about 120°C) shelf energy of about 125 J. In contrast, the F82H shows an extremely abrupt transition at about -50±10°C to an upper shelf energy of over 300 J, consistent with data reported elsewhere.[9] The DBTT indexed at 41J, T_{41}, is about 81°C higher in the HT9 (25°C versus -56°C for the F82H). However, the choice of 41J, where the fracture mode involves a mixture of cleavage and microvoid coalescence, as an index for a DBTT is arbitrary. Other DBTT values are obtained using alternate measures, such as: 1) 50% shear fracture appearance (34±5°C for the HT9 versus -55±5°C for the F82H); 2) 35 mils (0.89 mm) lateral expansion (119±5°C versus -56±5°C); and 3) 50% of the upper shelf energy (50±5 versus -50±5°C). A more physically meaningful index is at an absorbed energy level of 10 J, T_{10}, which has been found to approximately correspond to the onset of linear elastic fracture.[18] Remarkably, the T_{10} for F82H and HT9 are virtually the same, about -60±5°C.

A better physical measure of fracture resistance is the energy expended up to the initiation of crack extension. Since it is generally difficult to define the exact initiation point, the initiation energy (E_i) is usually defined as the energy absorbed at maximum load.[13] Figure 2b shows that the E_i for F82H also has an extremely abrupt transition compared to HT9. The DBTT based on the highest temperature for cleavage initiation (evident as a sharp drop in load in the load-time curve) in blunt notched Charpy impact tests is about 60±6 and -43±3°C, respectively, for HT9 and F82H, a difference of about 103°C.

Figure 2c shows the E-T curve for the MCVN tests. Here we have multiplied the actual E by a factor of 27 which
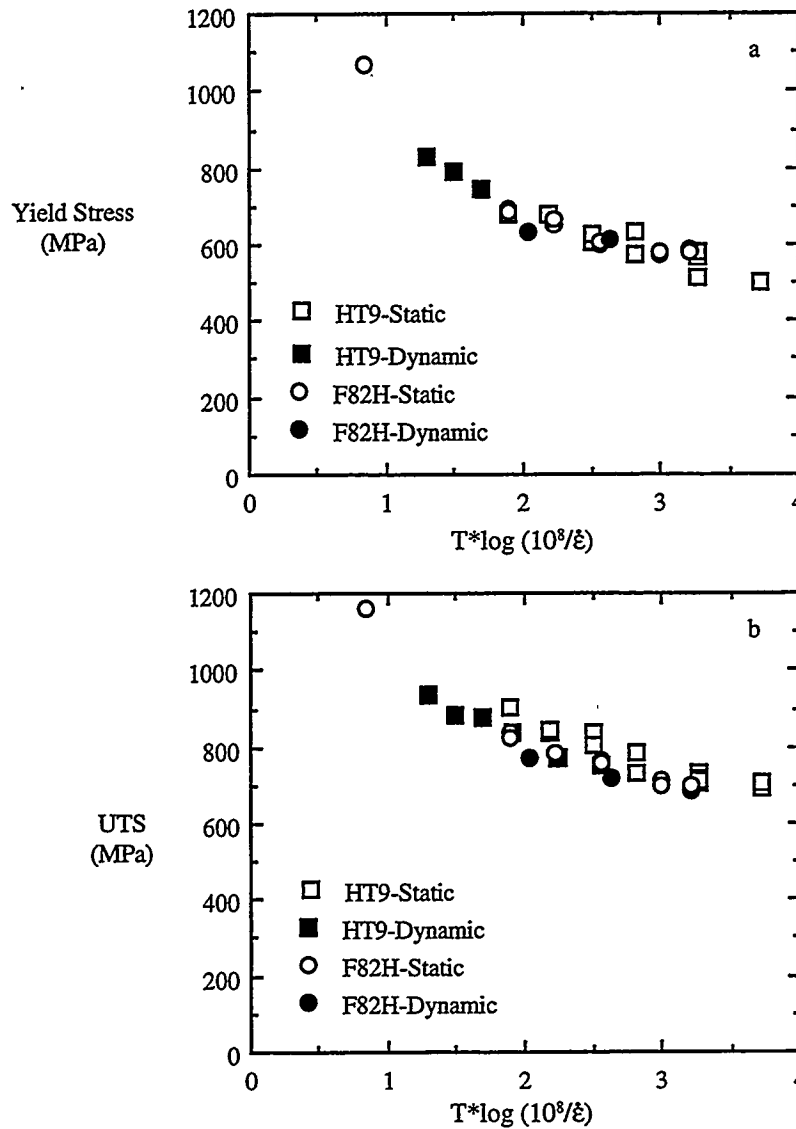
Figure. 1   Comparison of a) yield stresses and b) ultimate tensile strengths of HT9 and F82H as a function of strain rate compensated temperature.
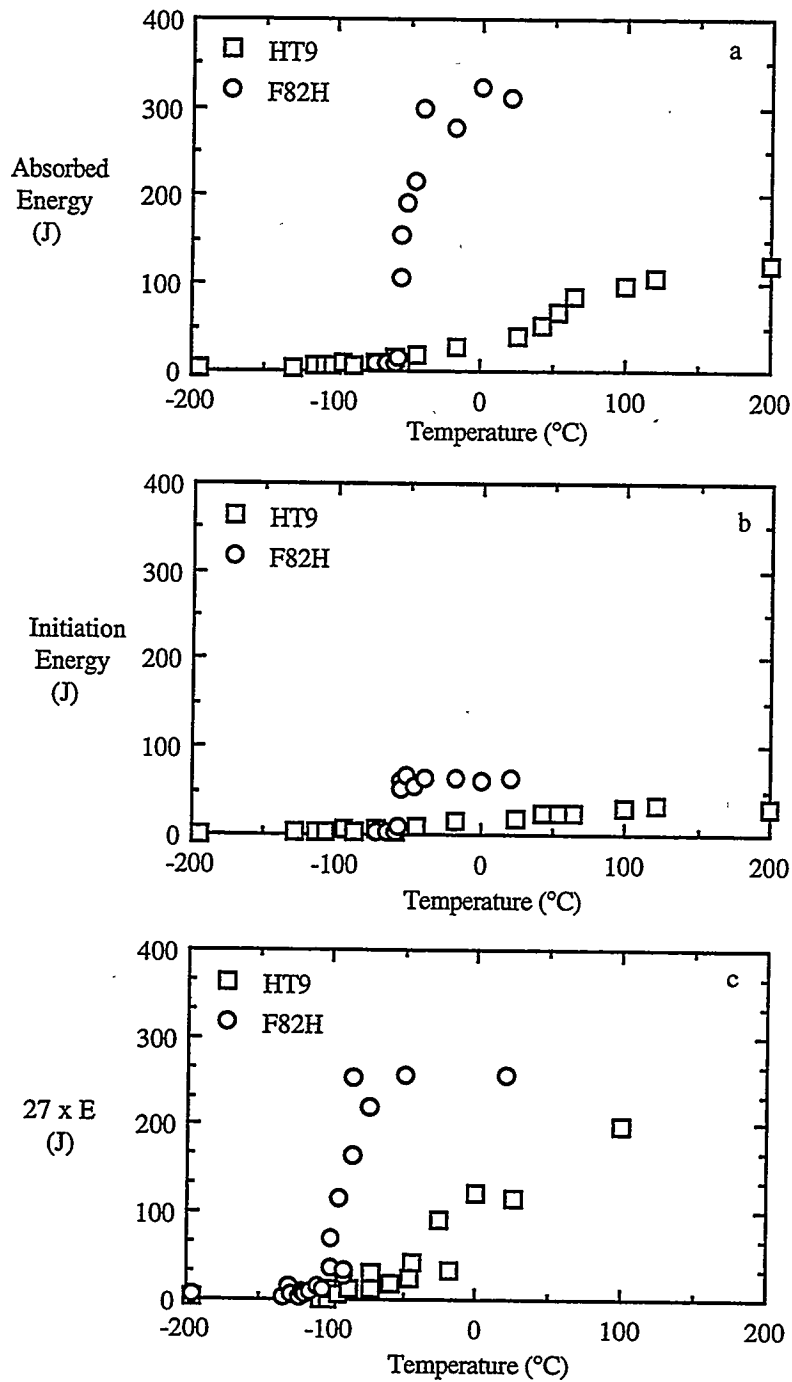
Figure 2   a) Charpy impact energy curves, b) initiation energies as a function of temperature for F82H and HT9 and c) Charpy impact energy curves for MCVN specimens.

is the appropriate continuum mechanics, self-similarity scaling factor for a 1/3-sized specimen. Based on the normalized 41J ($\approx$ 1.5 actual) index, the DBTT's for HT9 and F82H are -35$\pm$5 and -100$\pm$5°C, respectively. Thus, in addition to giving different absolute values of DBTT, the MCVN and CVN tests also yield somewhat different measures of the relative advantage of F82H based on the same normalized energy index, but for different geom-

etries — i.e., 65°C for the MCVN versus 81°C for the CVN. More elaborate interpretations of the MCVN data are available but will not be pursued here.

At this point it is important to reiterate that there is <u>no unique</u> DBTT, and to note that any measure of DBTT from the Charpy test is to some extent arbitrary and extrinsically mediated — that is, dependent on the details of this particular test as well as the basic properties of the material. However, among the <u>least</u> meaningful indices is 41J of total absorbed energy. In general 41J represents a non-unique combination of two different and, in themselves, not fully defined fracture processes.

The difference between E and E_i represents the energy dissipated during crack propagation. In the upper shelf regime, E is dominated (> 70%) by this propagation energy. However, ductile tearing in Charpy specimens occurs under enormously complex conditions of massive deformation, loss of crack tip and lateral constraint and out-of-plane deflection in the vicinity of the compressed region under the striker. Hence, it is not surprising that efforts to relate the upper shelf energy to more meaningful measures of fracture resistance, such as upper shelf initiation toughness and tearing modulus, have met with limited success.[19] A potentially better relationship might be obtained between upper shelf toughness and the initiation energy for ductile tearing, since this parameter avoids many of the complications noted above.

Fracture Toughness - While also beset with a number of questions concerning both measurement and application, fracture toughness clearly provides a far more meaningful and direct measure of the stress and strain capacity of cracked structures. The variation of static fracture toughness with test temperature for the two steels in this study is shown in Figure 3. We have included some recently published estimates of the upper shelf toughness data for F82H from Ref. 20. It is important to emphasize that the data in Figure 3 represent different measures of toughness (K_{Ic} and K_{Jc} and K_{JR})[1] based on, in a number of cases, small specimen tests that may not be strictly valid. However, our discussion will focus on a comparison of the overall K(T) curves rather than details of each data point. The HT-9 reaches an upper shelf toughness of about 200 MPa√m at about 20°C. The upper shelf static toughness of F82H is estimated to be about 250 MPa√m. Notably, the upper shelf, ductile initiation toughness advantage of roughly 25% for F82H versus HT9 compares to a factor of 3 in Charpy upper shelf energy. A fairer comparison would be based on the square root of the Charpy energy; on this basis the total energy and initiation energies would predict an F82H upper shelf toughness advantage of 70% and 40%, respectively.

It is also useful to characterize the transition temperatures indexed by toughness. While various indices could be chosen, fracture toughness is typically indexed at an elastic-plastic, cleavage-initiation level of 100 MPa√m. Unfortunately, there are only limited data in the transition regime, particularly for F82H. At -40°C the latter

---

1 Here J-values have been converted based on the elastic equivalent $K = \sqrt{JE'}$ where E' is the plane strain modulus.
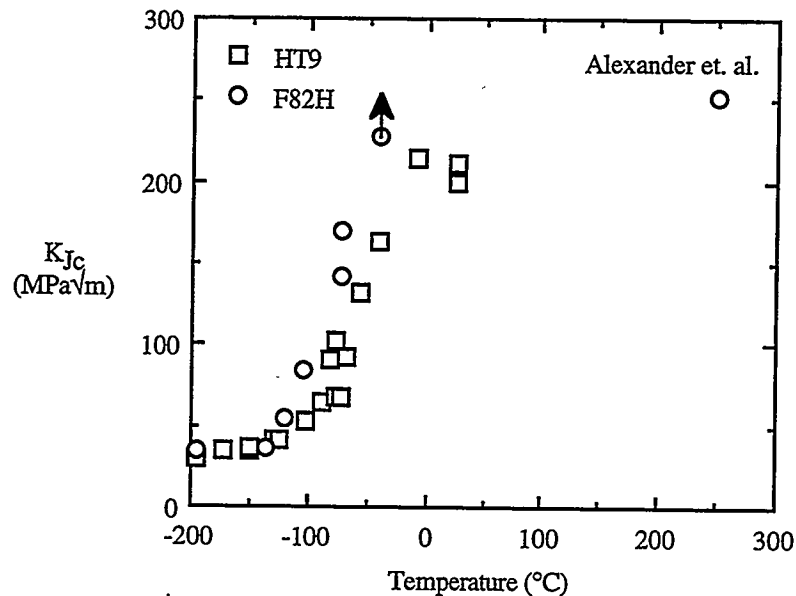
Figure 3   Comparison of static fracture toughness as a function of test temperature.

merely blunted up to the maximum available displacement. Hence, as indicated by the arrow, this represents a lower bound on the toughness in Charpy-sized specimens at this temperature; the value may be as high as the upper shelf toughness of about 250 MPa√m. Using these limited values as a guide, we estimate the 100 MPa√m transition temperature for F82H to be about -100°C±5°C, compared to -75°C ±10°C for HT9.

The variation of dynamic fracture toughness with test temperature as determined from instrumented PCCV tests is shown in Figure 4. As expected the dynamic loading rates have shifted the curves up in temperature. The F82H once again undergoes a very steep transition to an upper shelf toughness of about 310 MPa√m. There are insufficient data to establish an upper shelf for the HT9; however, the maximum toughness of 276 MPa√m suggests the relative advantage of F82H may be even smaller for dynamic toughness. A greater similarity of the behavior of the two materials is also reflected in the 100MPa√m transition temperature which is about 0°C for F82H compared to about 14°C for the HT9. The corresponding differences between dynamic and static transition temperatures at 100 MPa√m are about 89°C and 100°C for the HT9 and F82H, respectively. The shift in the dynamic versus static toughness curves at 100 MPa√m roughly coincides with the difference in temperatures at which the same value of σ_y is obtained in dynamic versus static tests.

Results — Quantitative Fractography

The SEM and confocal microscopy/fracture reconstruction (CM/FR) results are described below for various fracture mechanism regimes. In the fracture reconstructions, the fracture sequences as a function of crack tip
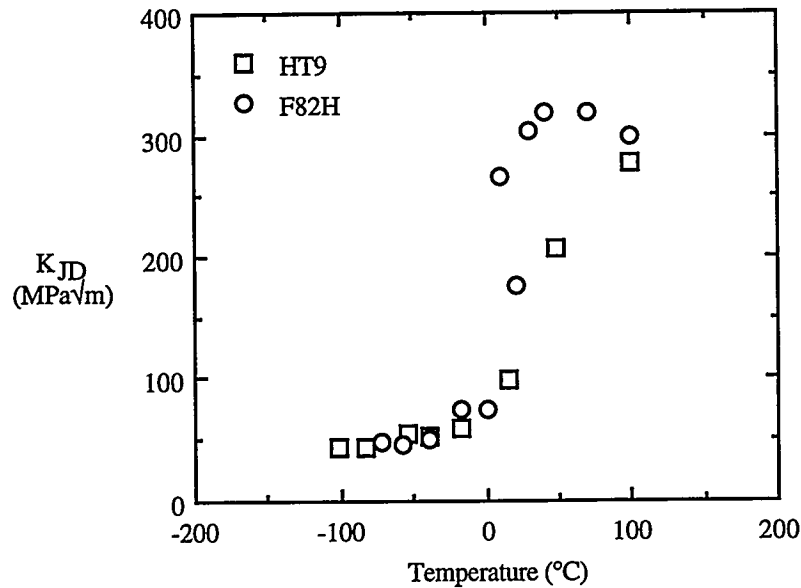
Figure 4   Comparison of dynamic fracture toughness as a function of test temperature

opening displacement (δ) are presented as views down onto the crack plane, often at the specimen center. Regions corresponding to material separation are shown in black and the regions corresponding to intact material are shown in white.

Lower Shelf /Lower Knee - Although not shown, the fracture processes for both HT9 and F82H are very similar on the lower shelf below about 45 MPa√m, with fracture in both alloys occurring by quasi-cleavage. Quasi-cleavage also dominates the lower knee regime in both steels.

Figure 5a shows a typical SEM fractograph corresponding to a static test of HT9 at -73°C in the lower knee region. Packets of cleavage facets are separated by thin regions of ductile tearing. The crack plane is characterized by an uneven surface, where out of plane areas of cleavage resulted in large multi- grain/packet "plugs" pulled out of "holes" in the conjugate surface. A corresponding CM/FR reconstruction of a 3PB specimen containing a crack with an a/W ≈ 0.4 is shown in Figure 6 for a toughness corresponding to a K_{Jc} of about 68 MPa√m. As the pre-crack blunts, stable multiple microcracking (black areas) initiates at a δ of about 16-17 μm and becomes completely unstable by about 20 μm. The region along the bottom is actually the specimen edge, which exhibits increased ductility, as would be expected. The critical condition appears to be controlled by a rapid coalescence of neighboring microcrack/tear ridge regions into a single or few large process zone cracks (PZC) extending over many PAG's. Assuming that $K_{J\delta} \approx \sqrt{2\sigma_y \delta * E'}$, critical crack opening of 19 μm corresponds to a $K_{J\delta}$ of about 81 MPa√m, in reasonable agreement with the mechanical test measurements of KJc at this temperature.
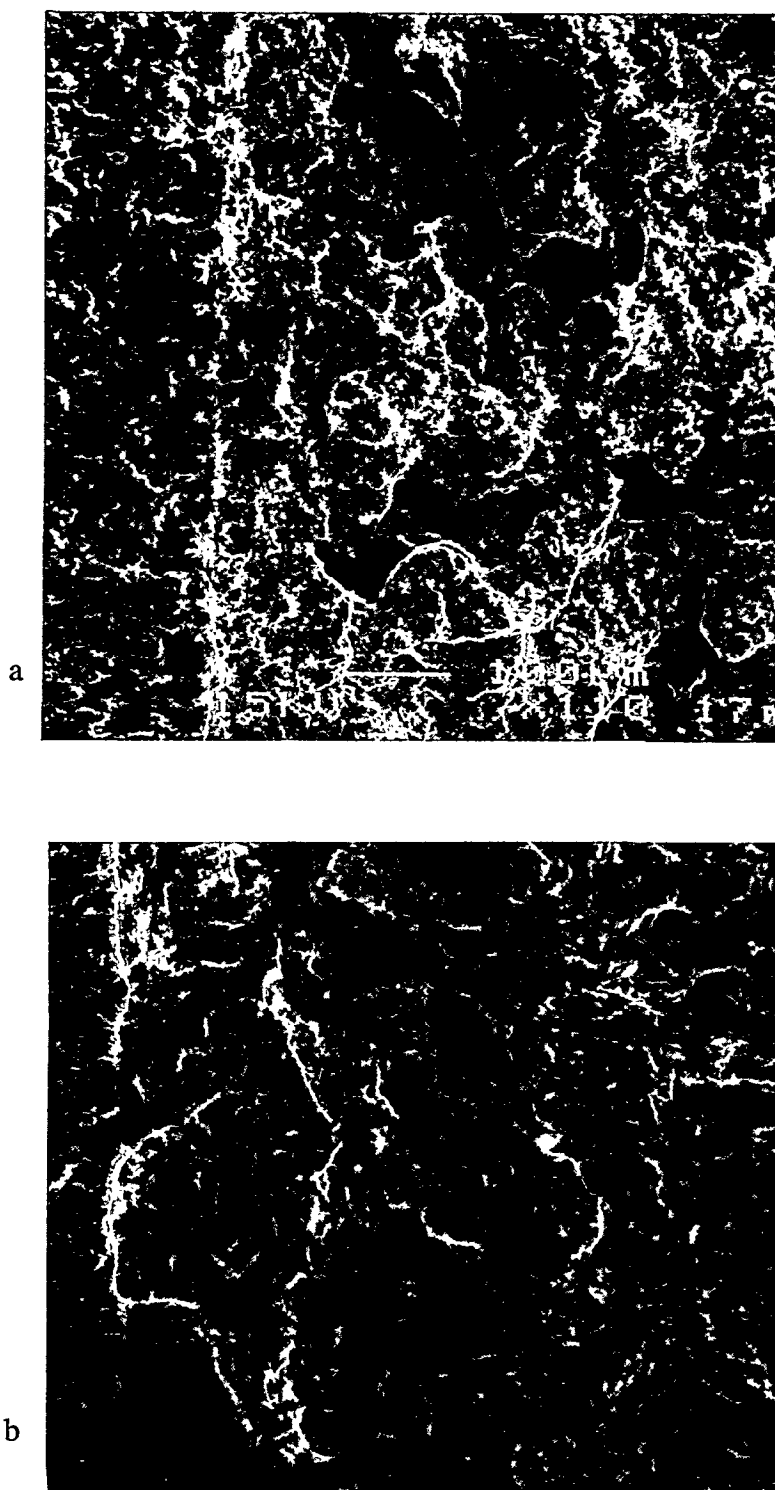
Figure 5   a) SEM fractograph of HT9 fracture specimen tested under static conditions at -73°C. b) SEM fractograph for an F82H specimen tested under dynamic conditions at -57°C.
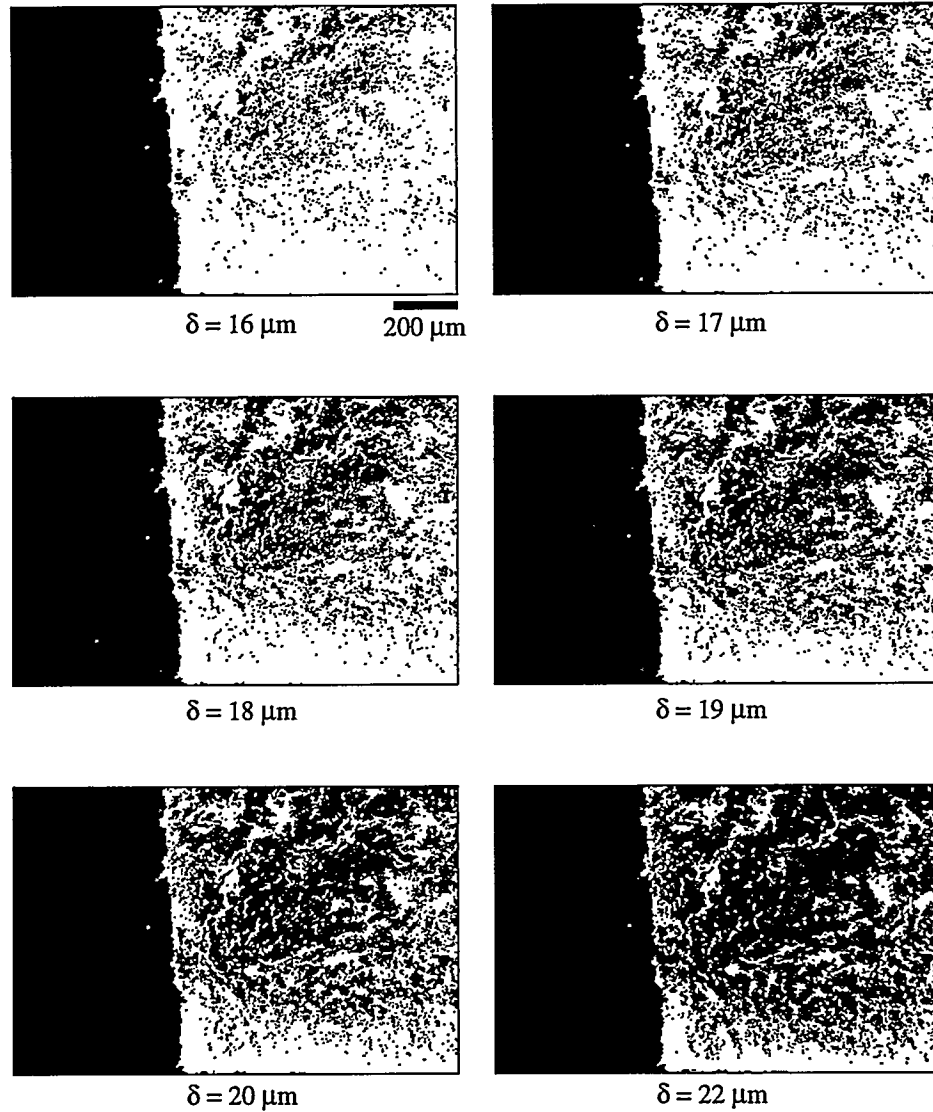
$\delta = 16\ \mu m$ 200 μm $\delta = 17\ \mu m$

$\delta = 18\ \mu m$ $\delta = 19\ \mu m$

$\delta = 20\ \mu m$ $\delta = 22\ \mu m$

Figure 6   Fracture surface reconstruction of an HT9 3pB specimen containing a crack with a/w=0.4 tested under static conditions at -73°C

Figure 5b shows a typical SEM fractograph corresponding to a dynamic test of F82H at -57°C, and Figure 7 shows a fracture reconstruction for a 3PB static test of F82H at -120°C. These tests represent K_{Jc}'s of about 47 and 60 MPa√m, respectively, closer to the lower shelf than the corresponding test on HT9. However, as evident in Figure 5b, the fracture surface is similar; i.e., again cleavage facets separated by tear ridges and a tortuous crack path. Moreover, as seen in Figure 7, a similar sequence of events leading to unstable fracture is observed: the crack blunts up to about 2-3μm prior to initiation of a small amount of microcracking, followed by unstable crack propagation between about 4-6 μm. A critical δ* of 5 μm corresponds to a $K_{J\delta}$ of about 68 MPa√m in reasonable agreement with the standard measures of K_{Jc} at this temperature (note that this specimen has an
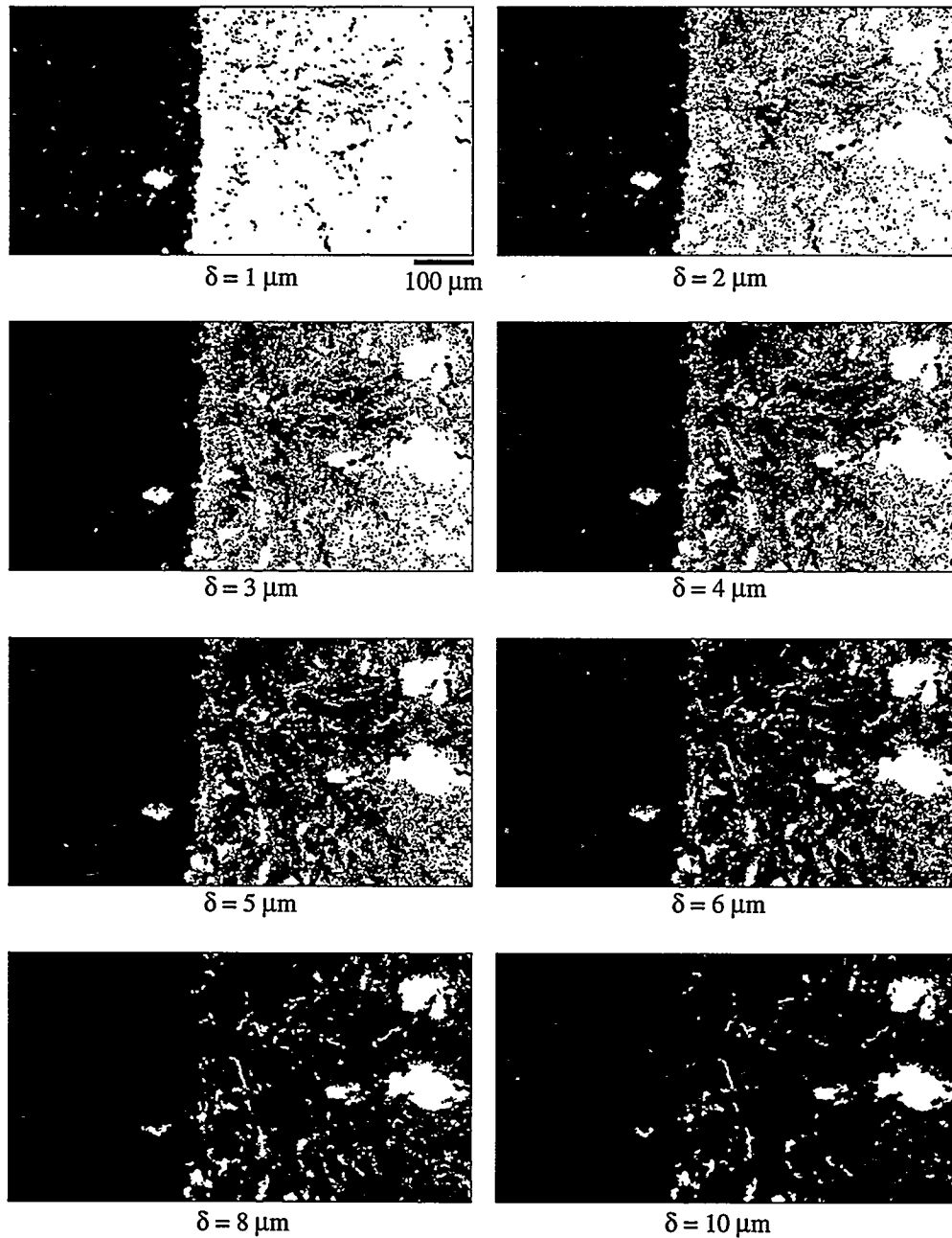
$\delta = 1\ \mu m$ 100 μm $\delta = 2\ \mu m$

$\delta = 3\ \mu m$ $\delta = 4\ \mu m$

$\delta = 5\ \mu m$ $\delta = 6\ \mu m$

$\delta = 8\ \mu m$ $\delta = 10\ \mu m$

Figure 7   Fracture reconstruction for an F82H 3pB specimen tested statically at -120°C

elastic component to K_{Jc} of 54 MPa√m). Note also that several intact ligaments remain in the crack wake (white regions at large δ in Figure 7). These correspond to "plugs" that have been geometrically interlocked in their "holes," resulting in formation of "hinge" like features propped up out of the fracture plane.

Transition region - As test temperature increases above the lower knee the same multiple microcrack coalescence instability process is observed. This is demonstrated by the CM/FR of a test on HT9 at -57°C shown in Figure 8.
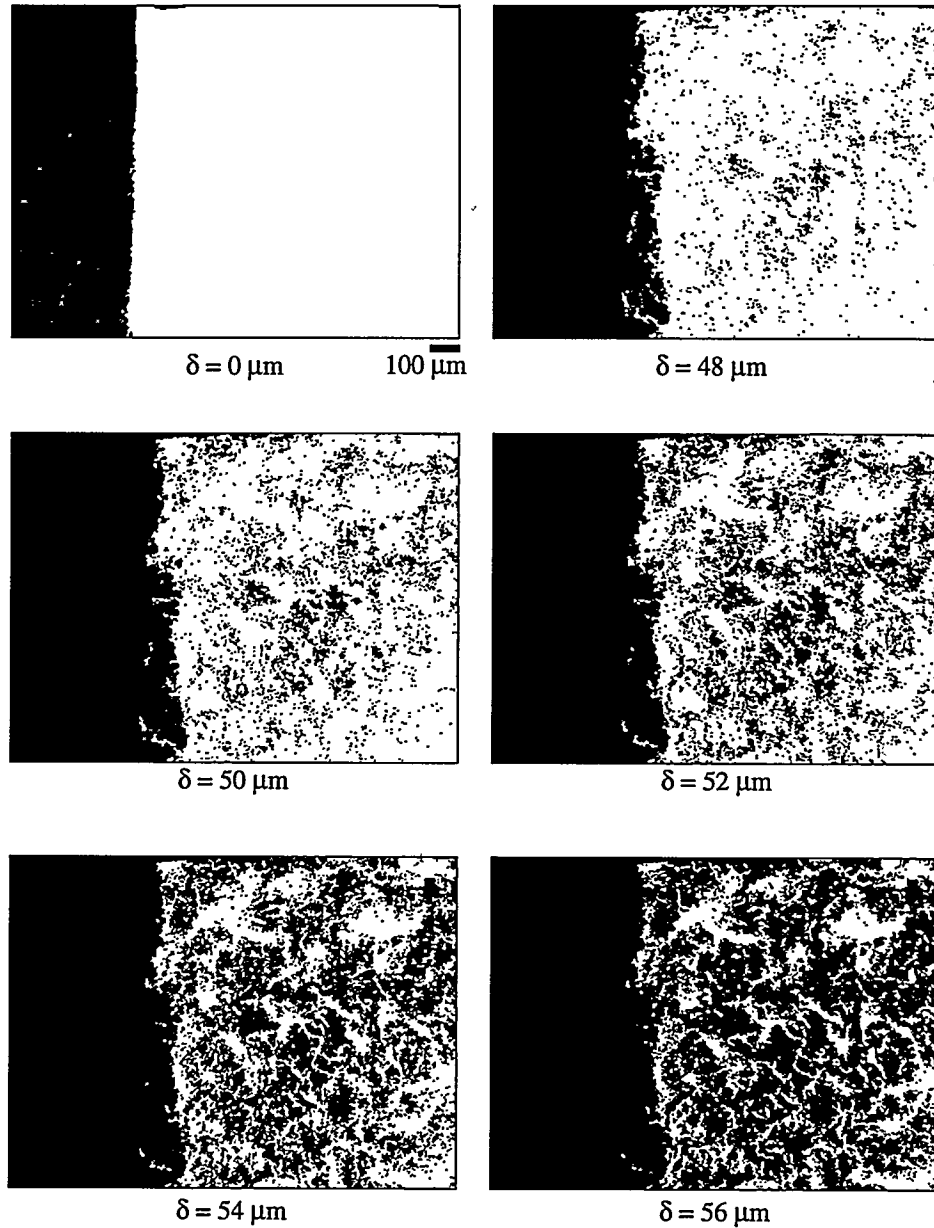
Figure 8   Fracture surface reconstruction for HT9 tested at -57°C.

However, the tear ridges become thicker as shown in the corresponding SEM micrographs in Figure 9, and more crack blunting is required to induce PZC instability conditions as seen in Figure 8. The critical crack opening of about 54 μm corresponds to a $K_{J\delta}$ of about 132 MPa√m, the same value measured during mechanical testing. A qualitatively identical sequence of events is observed for a static test on F82H at -73°C (not shown); in this case, the critical δ^* is about 65 μm corresponding to a $K_{J\delta}$ of about 141 MPa√m compared to a K_{Jc} of 142 MPa√m.

As shown in the SEM micrograph in Figure 10, by -40°C the fracture process in HT9 transforms to a mixture of
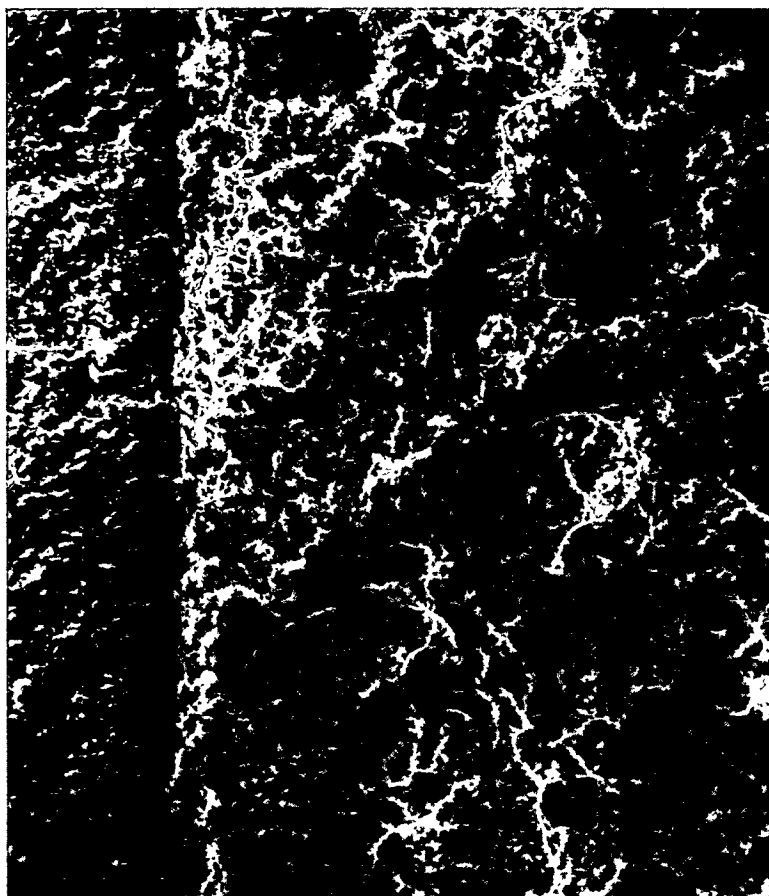
Figure 9   SEM micrograph of a region at the root of the pre-crack in HT9 tested at -57°C.

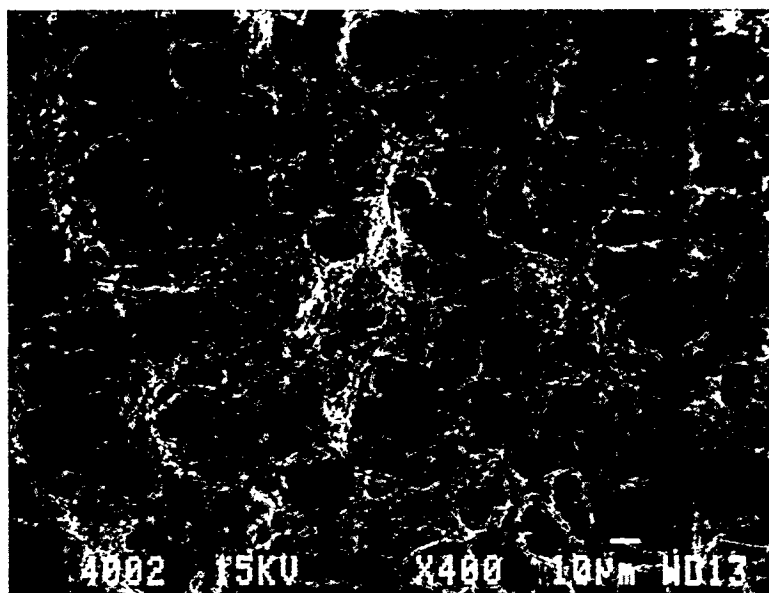Figure 10   SEM fractograph of HT9 fracture specimen tested under static conditions at -40°C.

predominantly quasi-cleavage with smaller regions of microvoid growth and coalescence in the fracture plane, in contrast to ductile shear fracture in the tear ridges. The CM/FR shown in Figure 11 demonstrates that the bridging ligaments provided by limited regions of microvoid coalescence also corresponds to the onset of stable crack propagation at an initiation δ^* of about 56 μm. The associated $K_{J\delta}$ is about 130 MPa$\sqrt{m}$ compared to a K_{Jc} of 140 MPa$\sqrt{m}$. The F82H does not show such a gradual transition to the upper shelf.

Upper shelf/knee region - The fraction of microvoid coalescence in HT9 increases with increasing temperature and becomes dominant on the upper shelf. The CM/FR in Figure 12 for static test at 20°C shows that crack growth in HT9 takes place by a repeated sequence of microvoid nucleation and growth terminated by coalescence with the blunting crack tip. Initiation is difficult to define in terms of δ^*, due to the subtle onset of crack advance. A slight increase in the rate of crack growth was detected at a δ^* of about 180 μm corresponding to a $K_{J\delta}$ of about
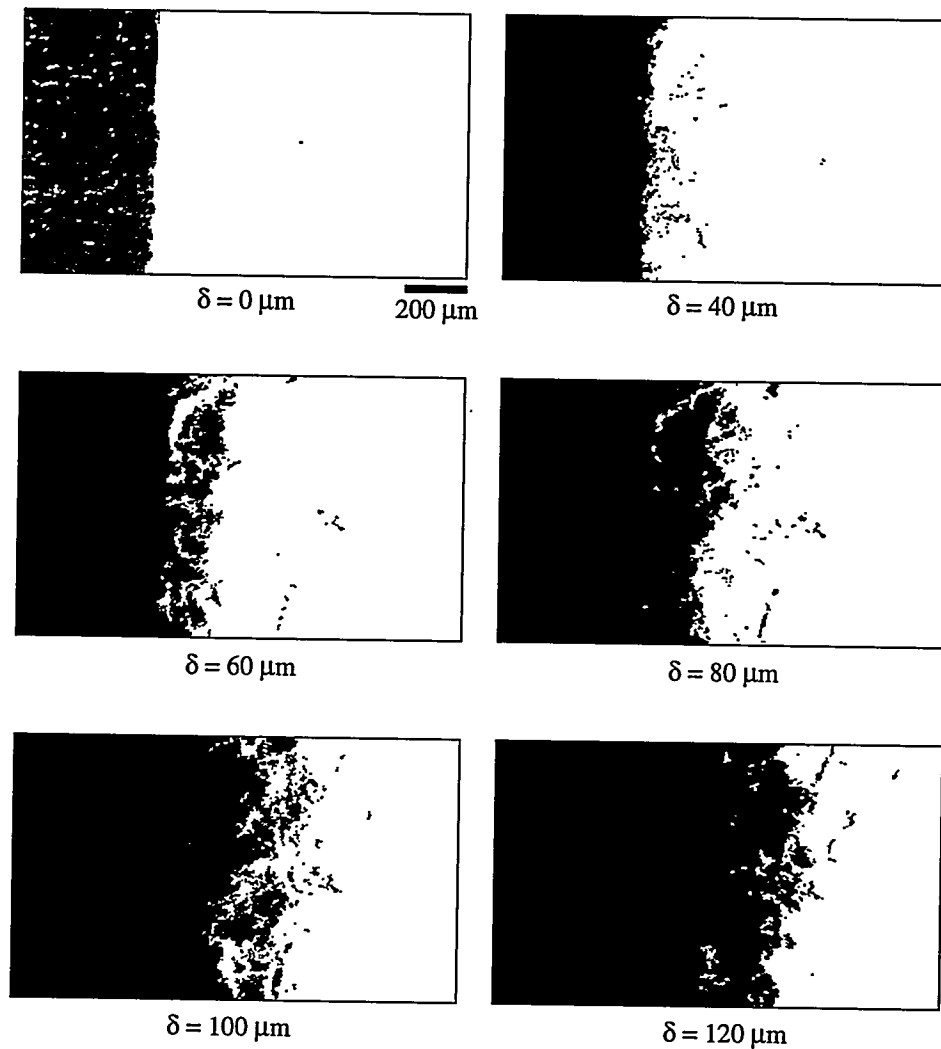

$\delta = 0 \ \mu m$ 200 μm $\delta = 40 \ \mu m$

$\delta = 60 \ \mu m$ $\delta = 80 \ \mu m$

$\delta = 100 \ \mu m$ $\delta = 120 \ \mu m$

Figure 11   Fracture surface reconstruction for HT9 tested under static conditions at -40°C

δ = 0 μm   200 μm   δ = 100 μm

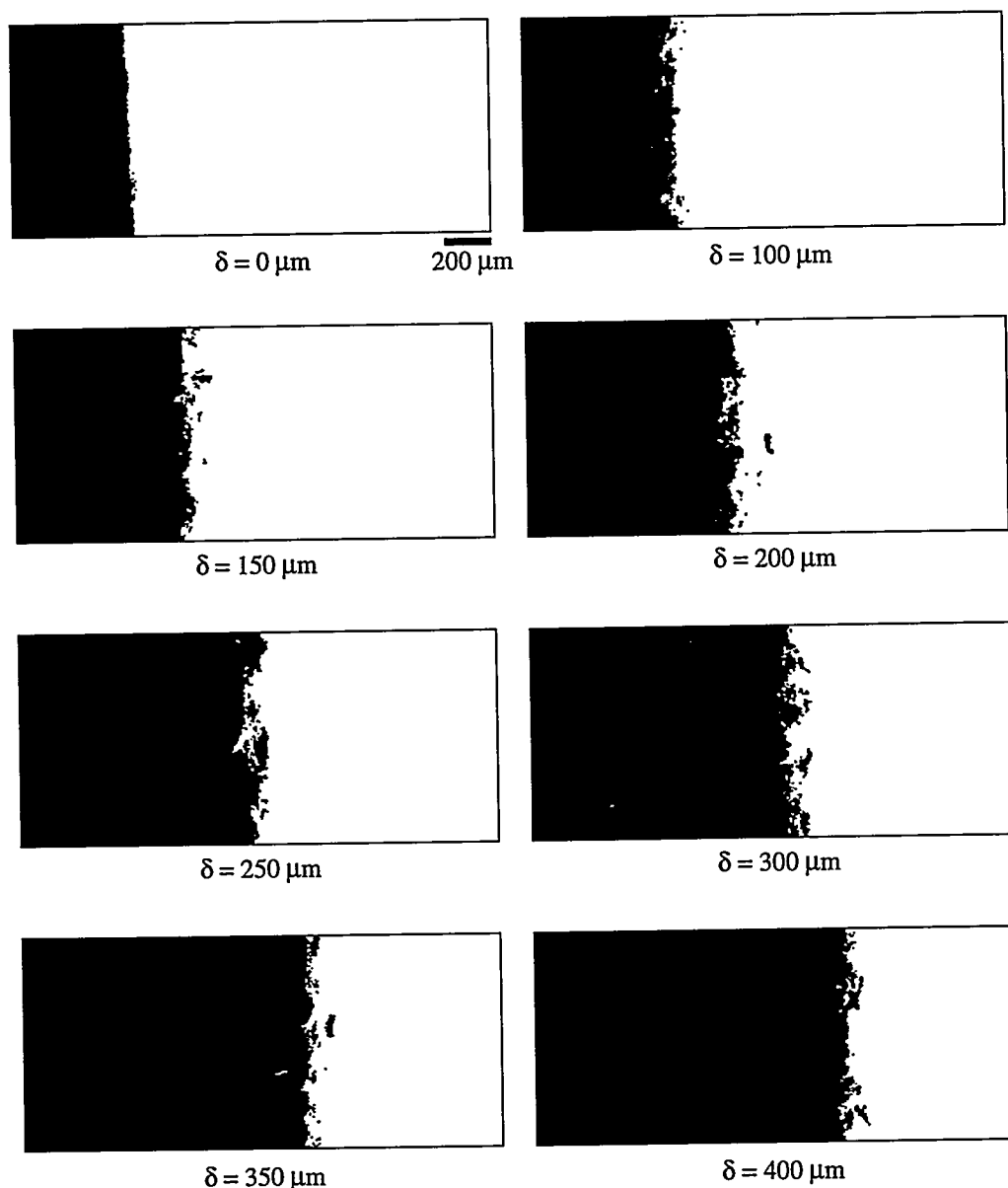δ = 150 μm   δ = 200 μm

δ = 250 μm   δ = 300 μm

δ = 350 μm   δ = 400 μm

Figure 12   Fracture surface reconstruction for HT9 tested under static conditions at 20°C

216 MPa√m compared to a K_{Jc} of about 214 MPa√m. However, only three points in the J-da plot lie to the right of the exclusion line, so that, while this value is reasonable, it is not technically valid. As shown in the SEM micrographs in Figure 13, even on the upper shelf, clusters of cleavage facets appear frequently at the center of the large microvoids, suggesting cleavage nucleation of these large microvoids. The growth of the cleavage-nucleated microvoids and linkage by regions with generally finer scale populations of microvoids formed on particles leads to coalescence. Upper shelf processes in F82H are qualitatively similar, as illustrated in the SEM micrograph in Figure 14 of the stretch zone region; this shows large voids associated with particles and cleavage facet clusters linked by regions of very fine microvoids leading to coalescence.
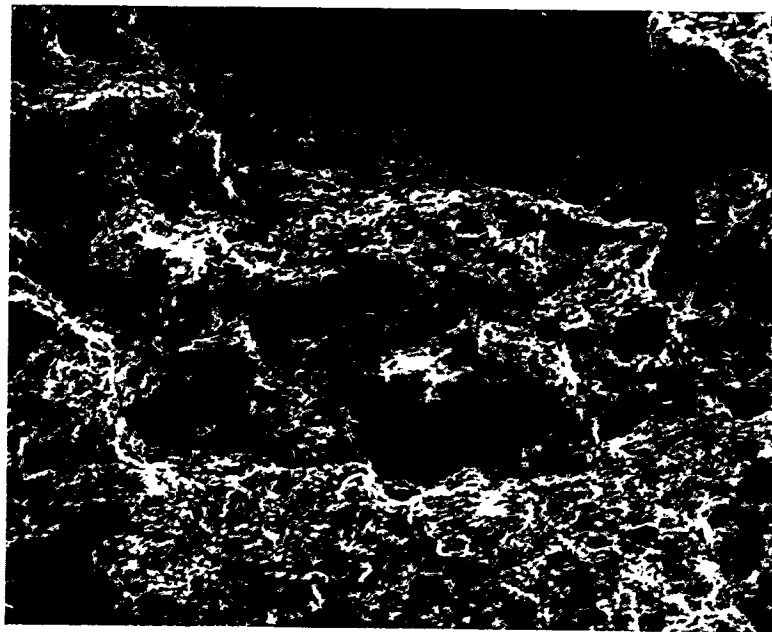
Figure 13   SEM fractograph of HT9 fracture specimen tested under static conditions at 20°C.
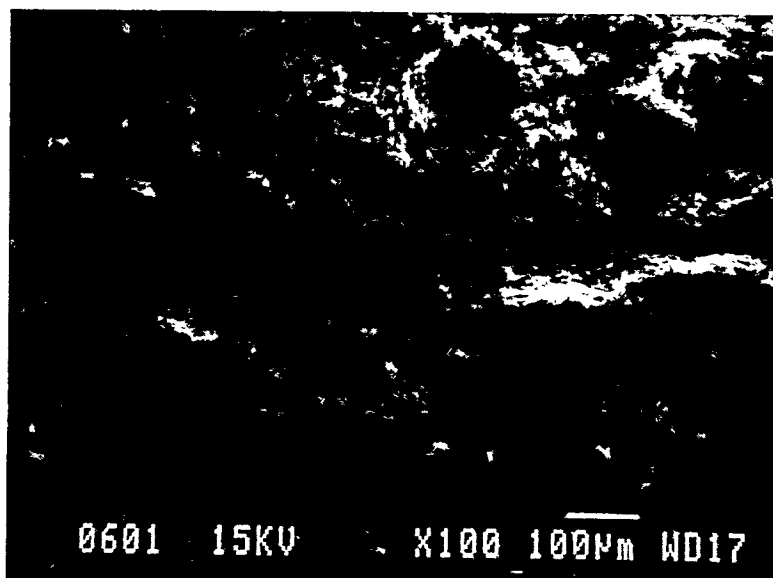

Figure 14   SEM fractograph of F82H fracture specimen tested under dynamic conditions at 100°C.

DISCUSSION

The results of the previous section can be summarized as follows:

- The behavior of HT9 and F82H is similar in the quasi-cleavage regime. As measured by transition temperatures, F82H has only slight advantages — i.e., transition temperatures ranging from about 0 to 25°C less than HT9 depending on the reference index.

- F82H can have higher fracture resistance in the upper shelf microvoid coalescence regime, ranging from factors of less than of 1.15 (dynamic toughness) to about 3 (Charpy upper shelf energy).

- The transition from quasi-cleavage to microvoid coalescence fracture is very gradual in HT9 and very abrupt in F82H.

- Primarily as a reflection of the width of the transition regime, mixed mode DBTT indexes show appreciably larger advantages for F82H, ranging from 65 to 175°C. However, the structural significance of these measures is not clear.

- Both steels manifest qualitatively similar fracture mechanisms in both quasi-cleavage and microvoid coalescence regions. The major differences appear to be: a) an intermediate mechanism regime unique to HT9, involving a mixture of the limiting micro-mechanisms; and b) slightly and significantly lower fracture resistance of the HT9 relative to F82H in the quasi-cleavage and microvoid coalescence regimes, respectively.

The basic micromechanics of the quasi-cleavage and microvoid coalescence regimes has been described elsewhere.[1,15] The more pertinent question in comparing these steels is — what gives rise to the large differences in the width of the transition regime? At lower temperatures in the mixed mode regime of HT9, small regions which ultimately fail by microvoid coalescence contribute to toughness by acting as bridging ligaments that can also sustain stable crack growth. The contribution of the microvoid coalescence regions gradually increases with increasing temperature to the point where the microvoid-associated ligaments give way to cleavage-facet-nucleated microvoids. The absence of the transition regime in F82H is not understood but might be rationalized on the basis of a synergistic interaction between microcrack formation and linking of microcrack-nucleated microvoids. Both processes appear to be more difficult in F82H compared to HT9. Thus the higher strains needed to form microcracks in F82H also promote the formation of more uniform dilational damage, lowering the peak stresses and preventing the nucleation of more microcracks. By definition, isolated microcracks transform to microvoids,
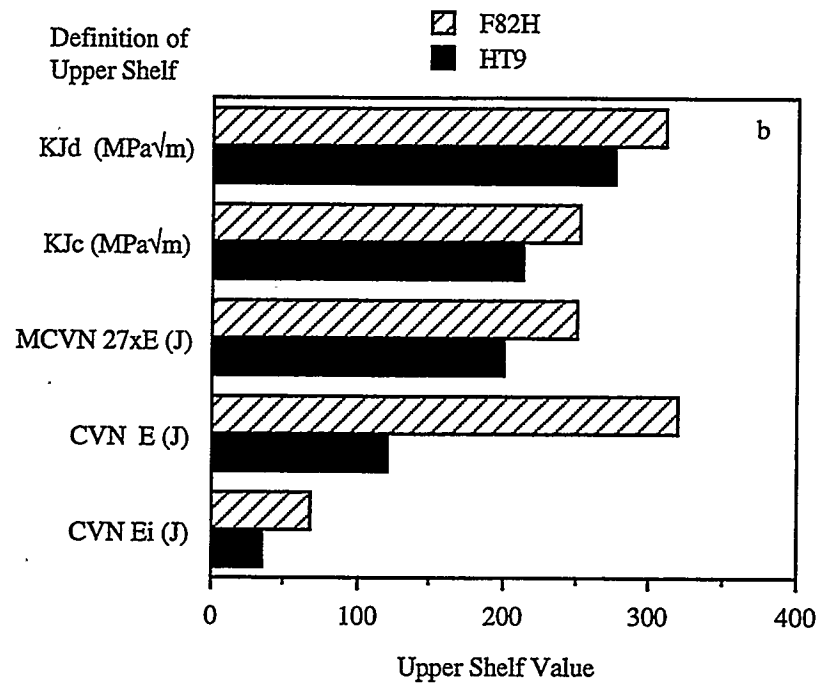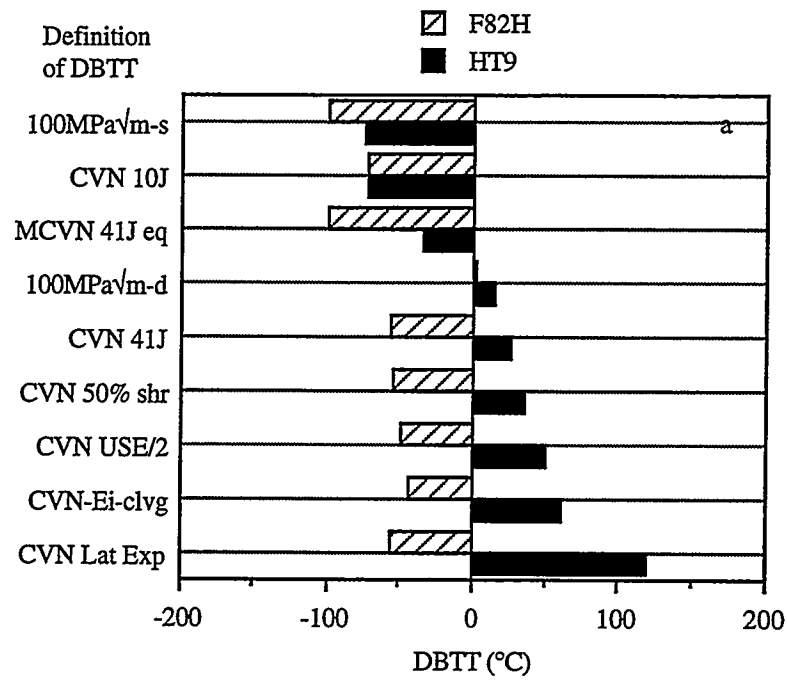
Figure 15   Comparison of a) transition temperatures and b) upper shelf values in F82H and HT9 for a variety of test types and indices.

rather than unstable or quasi-stable process zone cracks. More isolated microvoids also require larger strains to reach coalescence conditions, which may also be more inherently difficult in F82H. The larger strains lead to local (dilational) and global (large scale yielding) loss of constraint, further reducing microvoid growth rates and delaying coalescence. Thus, subtle difference in the underlying processes can lead to large differences in regions where they have the potential to interact.

An even more fundamental question is — what is the microstructural basis for these differences? While more detailed microstructural characterization will be needed, we believe the major difference is probably due to the relative compositions and heat treatments of the two alloys and the corresponding differences in carbide populations. The ratio of fine scale carbide formers — molybdenum + tungsten + vanadium — to carbon is about 8 for HT-9 compared to 22 for F82H. The corresponding ratio of chromium, which is associated with coarser carbides, to carbon is roughly similar: that is 53 for HT9 versus 80 for F82H. These compositional factors lead to a greater proportion of finer matrix and boundary carbides in F82H, and the lower C content results in an overall lower volume fraction of carbides. In addition, the HT9 heat treatment led to coarser boundary carbide distributions. The greater quantity of coarse carbides promote both quasi-cleavage microcrack nucleation and the nucleation of the finer scale secondary microvoids leading to coalescence of the large microvoids.

Details of the mechanisms aside, the results of this study clearly demonstrate the non-uniqueness of both absolute and relative values of the so-called DBTT. This is illustrated in Figure 15a, which compares the numerous measures of DBTT for the various indices described in the Results section for HT9 versus F82H. Variations of almost 200°C (e.g., tracking the solid bars from top to bottom) were found for HT9 depending on the specimen size and choice of reference index, while the variations for F82H were substantially less. Corresponding differences in material ranking by DBTT (solid versus hatched bars) ranged from relatively small (top of the bar chart) to more than 150°C (bottom of the bar chart) depending only on the reference index. Similar differences in the measures of upper shelf fracture resistance are shown in Figure 15b; again differences between HT9 and F82H (solid versus hatched bars) varied by factors of only slightly more than 1 to about 3. Clearly, a more quantitative and structurally relevant approach is needed.

CLOSING REMARKS

While simple standard test methods yield widely divergent measures of fracture resistance, even greater differences can be expected for actual structures characterized by complicated configurations and loading conditions. We believe that a much more rigorous and reliable approach to structural integrity assessment can be based on a combination of macromechanics and micromechanics; neither alone is sufficient.[1] The basic concept is to combine finite element simulations of the evolution of multiaxial crack tip stress and strain fields with local

measures of the conditions leading to crack extension (initiation or stable growth). The effects of variations in stress states can be directly modeled, even in complex geometries which deviate from small scale yielding conditions. This approach also opens the way to far more rigorous use of small specimens. Local measures of fracture resistance may involve simple stress-volume (distance) or strain-volume criteria or more complex statistical cleavage or microvoid growth models. Calibration of the fields and local fracture parameters to one, or ideally more than one, specimen geometry can be used to interpolate or extrapolate to other structurally relevant geometries. This approach can also be used to specify qualitative/ quantitative criteria for failure: elastic-plastic cleavage initiation at a specified toughness level corresponding to a specified stress and strain margin; the occurrence of some stable crack growth prior to cleavage instability; and ductile tearing. Not only would such criteria give physical relevance to specified safety margins, but they would also be readily incorporated into statistical/ probabilistic-based safety assessment. We believe that the local approach is critical to the intelligent and effective use of not only TM steels but also for essentially all other candidate structural materials for fusion applications.

FUTURE WORK

The work on F82H is continuing with an emphasis on further developing micromechanical models of quasi-cleavage and ductile fracture for this class of steels, and applying these models to failure prediction.

ACKNOWLEDGEMENTS

REFERENCES

1.   G. R. Odette, J. Nucl. Mater., Proceedings of ICFRM-6.

2.   G. R. Odette, B. L. Chao, G. E., Lucas, J. Nucl. Mater., Proceedings of ICFRM-6.

3.   G. R.Odette, G. E. Lucas, B. L. Chao, submitted to J. Nucl. Mater.

4.   M. Tamura, H. Hayakawa, M. Tanimura, A. Hishnuma, T. Kondo, J. Nucl. Mater. 141-143 (1986) 1067.

5.   Proceedings IEA Working Group Meeting on Ferritic/Martensitic Steels, ORNL, May 20-21, 1993.

6.   C. K. Elliott, G. E. Lucas, R.. Maiti, G. R.Odette, J. Nucl. Mater. 141/143 (1986) 439.

7.   G. R. Odette, G. E.Lucas, R.Maiti, J. W. Sheckherd, J Nucl. Mater, 122/123 (1984) 442.

8. Y. Kohno, D.Gelles, A. Kohyama, M. Tamura, A. Hishinuma, J. Nucl. Mater. 191/194 (1992) 868.

9. M. Tamura, H. Hayakawa, A. Yoshitake, A. Hishinuma, T. Kondo, J. Nucl. Mater. 155/157 (1988) 620.

10. R. L. Klueh, J.-J. Kai, D. J.Alexander, submitted to ASTM conference proceedings, Sun Valley, ID, 1994.

11. A. Kimura and H. Matsui, J. Nucl. Mater., Proceedings of ICFRM-6.

12. G. E. Lucas, G. R Odette, R. Maiti, J. W. Sheckherd, ASTM-STP-956, American Society for Testing and Materials, Philadelphia, PA (1987) 379.

13. W. L. Server, J. Test. and Eval., 6, 1 (1978) 29.

14. C. Elliott, M. Enmark, G. E. Lucas, G. R. Odette, A. Rowcliffe, J. Nucl. Mater. 179/181 (1991) 434.

15. K. Edsinger, G. R. Odette, G. E. Lucas, J. Nucl. Mater., Proceedings of the IEA International Symposium on Miniaturized Specimens for Testing of Irradiated Materials, Julich, Germany, 1994.

16. K. Edsinger, B. Wirth, G. R. Odette and G. E. Lucas, submitted to ASTM conference proceedings, Sun Valley, ID, 1994.

17. J. M. Steichen and J. A. Williams, J. Nucl. Mater. 57 (1975) 303.

18. G. R. Odette, P. M. Lombrozo, R. A. Wullaert, Effects of Radiation on Materials: 12th International Symposium, ASTM STP 870, F. A. Garner and J. S. Perrin, Eds., ASTM, Philadelphia, PA (1985) 840

19. S. T. Rolfe and J. M. Barsom, Fracture and Fatigue Control in Structures, Prentice Hall, New Jersey (1977) 174.

20. D. Alexander, J. E. Pawel, M. L. Grossbeck, A. F. Rowcliffe, submitted to ASTM conference proceedings, Sun Valley, ID, 1994.